Fuzzy Clustering and Active Contours for Histopathology Image Segmentation and Nuclei Detection

Adel Hafiane, Filiz Bunyak, and Kannappan Palaniappan⋆

Department of Computer Science,
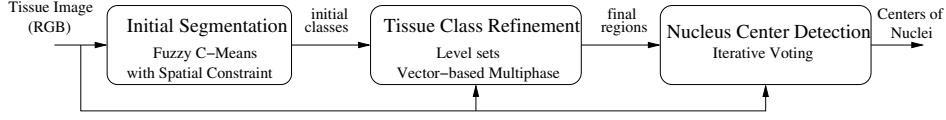University of Missouri-Columbia, Columbia, MO 65211 USA

Abstract. Histopathology imaging provides high resolution multispectral images for study and diagnosis of various types of cancers. The automatic analysis of these images can greatly facilitate the diagnosis task for pathologists. A primary step in computational histology is accurate image segmentation to detect the number and spatial distribution of cell nuclei in the tissue, along with segmenting other guiding structures such as lumen and epithelial regions which together make up a gland structure. This paper presents a new method for gland structure segmentation and nuclei detection. In the first step, fuzzy c-means with spatial constraint algorithm is applied to detect the potential regions of interest, multiphase vector-based level set algorithm is then used to refine the segmentation. Finally, individual nucleus centers are detected from segmented nuclei clusters using iterative voting algorithm. The obtained results show high performances for nuclei detection compared to the human annotation.

1 Introduction

The prostate cancer is a major health problem. The histopathologist study and diagnose prostate cancer using high resolution multispectral multimodal imaging of tissue biopsies. The diagnosis require highly skilled experts and is often a tedious task. Computer Assisted Diagnosis (CAD) approach helps to overcome this problem and provides new perspectives to develop algorithms for classification of histological images in a clinical setting. Automated quantitative grading of prostate cancer tissue patches that is beginning to compare favorably with visual analysis by experts for assigning a Gleason grade to histological imagery was demonstrated using a combination of low level image texture features and high level graph-based tissue architecture features [1]. The authors in [1] classify the prostate histology into four categories (Gleason grade 3 adenocarcinoma, grade 4 adenocarcinoma, benign epithelium and benign stroma). They use graph-based, morphological and textural features with support vector machine (SVM) to classify the different tissues. However, the architectural features

---

Tissue Image (RGB) → Initial Segmentation / Fuzzy C–Means with Spatial Constraint → initial classes → Tissue Class Refinement / Level sets / Vector–based Multiphase → final regions → Nucleus Center Detection / Iterative Voting → Centers of Nuclei

Fig. 1. Process flow

of gland structures including spatial distribution of cell nuclei and the arrangement of glands were determined using manual segmentation in [1]. Recently, semi-automated image segmentation algorithms requiring prior probability estimates for the lumen structures and pixel-wise classification were developed to facilitate the extraction of spatial arrangement information [2].

This paper presents robust image segmentation algorithm for histopathology imagery using a three steps process (Fig. 1). The fuzzy spatial clustering initialize the tissue class, then the vector-based multiphase level-sets with Beltrami color edge stopping function refine the segmentation. This process allows the extraction of nuclei, lumen and epithelial cytoplasm regions. The detection of individual nuclei centers is performed by iterative voting with oriented kernels.

The paper is organized as follows: Section 2 describes the Fuzzy C-means with spatial constraint algorithm, Section 3 presents the level sets multiphase scheme, and Section 4 describes the nuclei center detection. The evaluation process is explained in section 5, results are given in Section 6, and the conclusions in Section 7.

2   Fuzzy C-Means with Spatial Constraint

In this section we describe the method used to initialize the level set procedure. The FCM algorithm minimizes the objective function $J(U,V)$ which is defined by the sum of similarity measures. The objective function is given by

$$J(U,V) = \sum_{i=1}^{C} \sum_{j=1}^{N} u_{ij}^m \| \mathbf{x_j} - \mathbf{v_i} \|^2 \tag{1}$$

where $X = \{\mathbf{x_1}, \mathbf{x_2}, ..., \mathbf{x_N}\}$ denote the set of data (pixel feature vector). $V = \{\mathbf{v_1}, \mathbf{v_2}, ..., \mathbf{v_C}\}$ represents the prototypes, known as the clusters centers. $U = [u_{ij}]$ is the partition matrix which satisfies the condition: $\sum_i^C u_{ij} = 1 \ \ \forall j$ m is a fuzzifier which indicate the fuzziness of membership for each point. The FCM algorithm is based on an iterative process by minimizing the distance between each point and the prototypes. The objective function Eq. 1 does not incorporate any spatial information. It is shown that the spatial information brings more robustness and efficiency to the fuzzy c-means algorithm [3], where a second term to include the spatial information is incorporated in the FCM objective function. This is expressed by the following equation:

$$J_M(U,V) = \sum_{i=1}^{C} \sum_{j=1}^{N} u_{ij}^m \| \mathbf{x_j} - \mathbf{v_i} \|^2 + \alpha \sum_{i=1}^{C} \sum_{j=1}^{N} u_{ij}^m e^{-\sum_{k \in \Omega} u_{ik}^m}$$

where Ω is a set of neighbors. The parameter α is a weight that controls the influence of the second term (spatial information). The objective function (2) has two components. The first component is the same as FCM, the second is a penalty term. This component reaches a minimum when the membership value of neighbors in a particular cluster is large. The optimization of (2) with respect to U was solved by using Lagrange multiplier technique. The obtained membership update function is given by

$$u_{ij} = \frac{1}{\sum_{p=1}^{C}\left(\frac{\|\mathbf{x_j}-\mathbf{v_i}\|^2+\alpha e^{-\sum_{k\in\Omega}u_{ik}^m}}{\|\mathbf{x_j}-\mathbf{v_p}\|^2+\alpha e^{-\sum_{k\in\Omega}u_{pk}^m}}\right)^{\frac{1}{m-1}}} \qquad (2)$$

The neighboring membership values (u_{pk}) influence u_{ij} to follow the neighborhood behavior. For instance if a given point has a high membership value to a particular cluster and its spatial neighbors have small membership values to this cluster, the penalty term plays the role to force the point to belong to the same cluster as its neighbors. The weight α controls the importance of the regularization term. The prototype update equation is the same as standard FCM.

$$v_i = \frac{\sum_{j=1}^{N} u_{ij}^m x_j}{\sum_{j=1}^{N} u_{ij}^m} \qquad (3)$$

The spatial constraint FCM (SCFCM) algorithm preforms the same steps as the original fuzzy c-means algorithm but the membership function is computed according to equation 2.

3   Multiphase Vector-Based Active Contours

In [4], Chan and Vese presented a multiphase extension of their two-phase level set image segmentation algorithm [5]. The multiphase approach enable efficient partitioning of the image into n classes using just $log(n)$ level sets without leaving any gaps or having overlaps between level sets. This ensures that each pixel is properly assigned to a unique class during the segmentation process. The Chan and Vese multiphase level set image segmentation approach involves minimization of a reduced or weak Mumford-Shah functional $F_n(\mathbf{c},\Phi)$, otherwise referred to as a *minimal partition* Mumford-Shah functional [6]:

$$F_n(\mathbf{c},\Phi) = \underbrace{\sum_{1\le i\le n=2^m} \lambda_i \int_\Omega (u_0 - c_i)^2 \chi_i\, d\mathbf{x}}_{\text{Energy Term}}$$

$$+ \underbrace{\sum_{1\le i\le n=2^m} \mu_i \int_\Omega |\nabla\chi_i|}_{\text{Length Term}} \qquad (4)$$

where n is the total number of classes associated with m level set functions, u_0 is the gray-level image being segmented, Φ is a vector of level set functions, $\mathbf{c}$ is a vector of mean gray-level values (i.e., $c_i = mean(u_0)$ of class or phase i), χ_i is the characteristic function for each class i represented by the associated Heaviside functions $H(\phi_i)$, and $(\lambda_i,\ \mu_i)$ are constants associated with each energy and length term of the functional $F_n(\mathbf{c}, \Phi)$.

In order to simplify computation of the length term in the above reduced Mumford and Shah energy function, we replace the measure of the characteristic functions by the sum of the length of the zero-level sets of ϕ_i, $\sum_{1 \leq i \leq m} \mu_i \int_\Omega |\nabla H(\phi_i)|$.

In order to exploit the edge information between different regions as in [7,8] we use a geodesic length measure, $\sum_{1 \leq i \leq m} \mu_i g(\mathbf{u_0}) \int_\Omega |\nabla H(\phi_i)|$ [9], which is basically length term weighted by an edge stopping function $g(\mathbf{u_0})$. This addition helps contours snap to the image edges and is useful to refine the segmentations of boundaries, particularly for nuclei. While edge stopping functions for single channel images are well defined, generalization to multi-channel images such as color histopathology images are not straight forward. Here as in [10] we use an edge stopping function obtained from Beltrami color metric tensor explained further below. Chan and Vese also extended their two-phase level set image segmentation algorithm for scalar valued images to vector-valued images such as color or multispectral images [11] where the image is partitioned into piecewise constant vectors in the spirit of spatially-based vector quantization. In this paper we combine the multiphase approach with the feature vector approach to handle both multiple image classes and vector-valued imagery such as segmenting color or multispectral images.

In the case of histopathology imaging derived from H&E stained cancer tissue biopsies four image classes have been shown to produce good feature sets for image classification-based cancer grading [1]. For the two level set case (i.e., $m = 2$) the image domain Ω is partitioned into *at most* four classes as shown in Fig. 2. Let $\mathbf{c} = \{\mathbf{c_{00}}, \mathbf{c_{01}}, \mathbf{c_{10}}, \mathbf{c_{11}}\}$ represent the set of average image feature
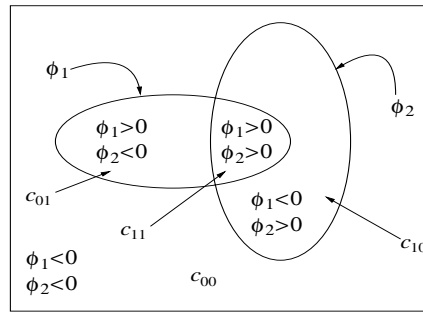
Fig. 2. A four-phase level set partitioning, with two level set functions ϕ_1 and ϕ_2, for segmenting vector-image $\mathbf{u_0}$, $\mathbf{c} = \{c_{00}, c_{01}, c_{10}, c_{11}\}$ represents the set of features vector averages for various phases, $H(\phi_1)$ and $H(\phi_2)$ are the Heaviside functions associated with each level set function

vectors (ie three channel color) within each class or phase $\mathbf{c_{ij}}$, and $\Phi = (\phi_1, \phi_2)$ represent the two level set functions. Our proposed extension for a multiphase vector-based energy functional $F_n(\mathbf{c}, \Phi)$ is defined as,

$$
\begin{aligned}
F_n(\mathbf{c}, \Phi) = & \lambda_1 \int_\Omega \| \mathbf{u_0} - \mathbf{c_{00}} \|^2 \ (1 - H(\phi_1))(1 - H(\phi_2)) d\mathbf{x} \\
& + \lambda_2 \int_\Omega \| \mathbf{u_0} - \mathbf{c_{01}} \|^2 \ (1 - H(\phi_1))H(\phi_2) \ d\mathbf{x} \\
& + \lambda_3 \int_\Omega \| \mathbf{u_0} - \mathbf{c_{10}} \|^2 \ H(\phi_1)(1 - H(\phi_2)) \ d\mathbf{x} \\
& + \lambda_4 \int_\Omega \| \mathbf{u_0} - \mathbf{c_{11}} \|^2 \ H(\phi_1)H(\phi_2) \ d\mathbf{x} \\
& + \sum_{1 \leq i \leq m} \mu_i \ g(\mathbf{u_0}) \ |\nabla H(\phi_i)|
\end{aligned}
\tag{5}
$$

The Euler-Lagrange equations are obtained by minimizing Eq. 5 and embedding $\mathbf{c}$ and Φ in a dynamical system as [4]

$$
\begin{aligned}
\frac{d\phi_1}{dt} = & \delta(\phi_1)\Big\{ \mu_1 \ g(\mathbf{u_0}) \ \mathrm{div}\big(\frac{\nabla \phi_1}{|\nabla \phi_1|}\big) \\
& - \big\{(\lambda_1 \| \mathbf{u_0} - \mathbf{c_{11}} \|^2 - \lambda_3 \| \mathbf{u_0} - \mathbf{c_{01}} \|^2)H(\phi_2) \\
& + (\lambda_2 \| \mathbf{u_0} - \mathbf{c_{10}} \|^2 - \lambda_4 \| \mathbf{u_0} - \mathbf{c_{00}} \|^2)(1 - H(\phi_2))\big\}\Big\}, \\
\frac{d\phi_2}{dt} = & \delta(\phi_2)\Big\{ \mu_2 \ g(\mathbf{u_0}) \ \mathrm{div}\big(\frac{\nabla \phi_2}{|\nabla \phi_2|}\big) \\
& - \big\{(\lambda_1 \| \mathbf{u_0} - \mathbf{c_{11}} \|^2 - \lambda_2 \| \mathbf{u_0} - \mathbf{c_{10}} \|^2)H(\phi_1) \\
& + (\lambda_3 \| \mathbf{u_0} - \mathbf{c_{01}} \|^2 - \lambda_4 \| \mathbf{u_0} - \mathbf{c_{00}} \|^2)(1 - H(\phi_1))\big\}\Big\}
\end{aligned}
\tag{6}
$$

where $\mathbf{c_{ij}}$ is the mean vector of all pixel-based vectors associated with each class or phase.

$$
\mathbf{c_{11}} = \frac{\int_\Omega \mathbf{u_0}\, H(\phi_1)\, H(\phi_2)\, d\mathbf{x}}{\int_\Omega H(\phi_1)\, H(\phi_2)\, d\mathbf{x}} \quad
\mathbf{c_{10}} = \frac{\int_\Omega \mathbf{u_0}\, H(\phi_1)\, (1 - H(\phi_2))\, d\mathbf{x}}{\int_\Omega H(\phi_1)\, (1 - H(\phi_2))\, d\mathbf{x}}
$$

$$
\mathbf{c_{01}} = \frac{\int_\Omega \mathbf{u_0}\, (1 - H(\phi_1))\, H(\phi_2)\, d\mathbf{x}}{\int_\Omega (1 - H(\phi_1))\, H(\phi_2)\, d\mathbf{x}} \quad
\mathbf{c_{00}} = \frac{\int_\Omega \mathbf{u_0}\, (1 - H(\phi_1))\, (1 - H(\phi_2))\, d\mathbf{x}}{\int_\Omega (1 - H(\phi_1))\, (1 - H(\phi_2))\, d\mathbf{x}}
$$

and $\delta(\phi_k) = H'(\phi_k)$ is the Dirac delta function. For numerical stability of the delta function, Chan and Vese propose using a regularized Heaviside function

$$
H_{2,\epsilon}(x) = \frac{1}{2}\Big[1 + \frac{2}{\pi}\Big\{tan^{-1}\big(\frac{x}{\epsilon}\big)\Big\}\Big] \quad with \quad \delta_\epsilon(x) = \frac{1}{\pi}\frac{\epsilon}{\pi^2 + \epsilon^2}
$$

The motivation for using a multiphase, rather than a two-phase, level set framework is to accurately detect adjacent regions that meet at a junction (i.e., the triple junction in [4]). However, as the number of regions grows exponentially with the

number of level set functions, its best to use a small set of level set functions (typically two or three or equivalently, four or eight regions, respectively).

Color Edge Strength: Although the spatial gradient for single channel images lead to well defined edge operators, edge detection in multi-channel images (as color edge strength in histopathology images) is not straight forward to generalize since gradients in different channels can have inconsistent orientations. The main issue in multi-dimensional gradient methods is the combination of the individual channel gradients into a final multi-dimensional gradient. Simple methods use operations such as sum, weighted sum, max, min etc. to produce the final multi-dimensional/color gradients. But the summation of the individual channel gradients discard the correlation between the channels and may result in cancellation effects [12]. To avoid this problem, here we use an edge stopping function obtained from Beltrami color metric tensor $\mathcal{E}$ Eq. 7. The Beltrami color metric tensor operator for a 2D color image defines a metric on a two-dimensional manifold $\{x, y, R(x, y), G(x, y), B(x, y)\}$ in the five-dimensional spatial-spectral space $\{x, y, R, G, B\}$.

$$\mathcal{E} = \begin{bmatrix} 1 + \sum_{i=R,G,B} \left(\frac{\partial \mathbf{I}_i}{\partial x}\right)^2 & \sum_{i=R,G,B} \frac{\partial \mathbf{I}_i}{\partial x} \frac{\partial \mathbf{I}_i}{\partial y} \\ \sum_{i=R,G,B} \frac{\partial \mathbf{I}_i}{\partial x} \frac{\partial \mathbf{I}_i}{\partial y} & 1 + \sum_{i=R,G,B} \left(\frac{\partial \mathbf{I}_i}{\partial y}\right)^2 \end{bmatrix} \tag{7}$$

An edge stopping function on color image can be defined using $\mathcal{E}$ as:

$$g(\mathbf{I}) = exp(-abs(\mathbf{det}(\mathcal{E}))) \tag{8}$$

4   Nucleus Center Detection

The shape and arrangement of glandular and nuclear structures within a histological image region is related to tissue type and can be used in classification between Gleason grades [1]. In [1] graphs describing the spatial arrangement of the nuclei (i.e. Delaunay triangulation of nuclei centers) are used in Gleason grade classification along with other features. The module described in this section automatizes detection of individual nucleus centers from the nuclei clusters segmented as in previous section. The technique used is based on iterative voting using the oriented kernels approach described in [13, 14].

The approach detects nucleus centers from incomplete boundary information through voting and perceptual grouping. The method applies a series of cone-shaped kernels (Figure 3) that vote iteratively along the radial or tangential directions [13]. The iterative approach refines the center of mass at each iteration until it converges to a focal response. At each iteration and location on the contour the voting kernel is aligned along the maximum response of the voting space. Additionally, the shape of the kernel is refined and focused within the iterative process. This technique has been chosen because of its noise immunity.

Figure 4 shows the evolution of the voting landscape $\mathbf{V}(i, j)$ and the resulting centers for two sample images, a synthetic test image, and a nucleus cluster image.
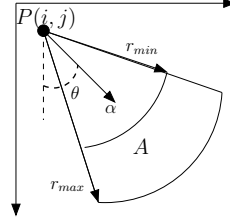
**Fig. 3.** Cone shaped kernel and the voting area A

(a)   (b)   (c)   (d)
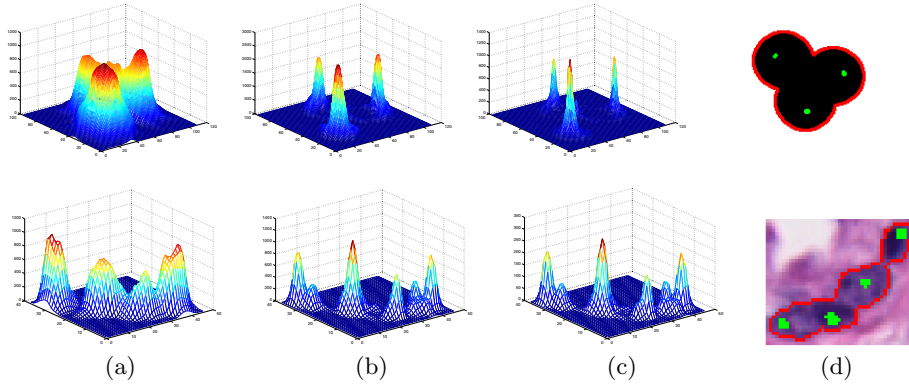
Fig. 4. Evolution of the voting landscape $\mathbf{V}(i,j)$ and the resulting centers for a synthetic image (top), and a nucleus cluster image (bottom). (a) iteration=1, (b) iteration=5, (c) iteration=10, (d) nucleus contours (red) and centers (green) superimposed on the original image.

5   Evaluation

The evaluation module compares nucleus center detection results to the ground truth (GT) annotated by the expert and computes some statistical measures. Detected centers are matched to ground truth centers using our automatic correspondence analysis algorithm. Automated correspondence analysis is critical in reliable evaluation, since statistics based on number of detected and ground truth centers can be misleading, and manual comparison of the detection results to the ground truth is labor intensive and often subjective.

Our correspondence analysis supports other detected-to-ground match types besides one-to-one matching such as: many-to-one, one-to-many, one-to-none, or none-to-one, that result from fragmentation, merge (under-segmentation of nuclei clusters), false detection, and missed center respectively. Major steps of the proposed analysis scheme are summarized below.

1. Distance matrix computation.
2. Absolute match pruning.
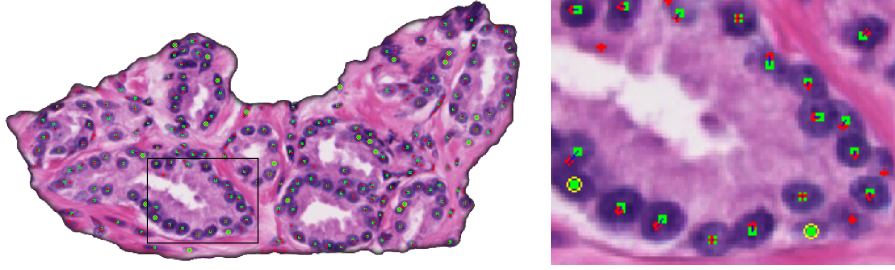
Fig. 5. Correspondence of detected and ground truth centers. Image on the right is zoomed from the marked region of the image on the left. In both images, detected centers and ground truth centers are marked as red pluses and green squares respectively. Blue lines link matching centers, yellow circles mark missed centers.

3. Bi-directional relative match pruning.
4. Match classification.

The Euclidean distance between every detected point to every ground truth point is computed and stored in a $n_D \times n_G$ distance matrix D where n_D is the number of detected centers and n_G is the number of ground truth centers. An additional $n_D \times n_G$ match matrix M is formed and initially set to 1.

Final correspondences are determined after two types of match pruning, absolute and relative. During absolute pruning, matches whose distances are higher than the maximum nucleus radius R_{max} are pruned by setting corresponding elements in M to 0:

$$D(d_i, g_j) > R_{max} \implies M(d_i, g_j) = 0 \qquad d_i \in 1..n_D, g_j \in 1..n_G \qquad (9)$$

During relative pruning, for each detected center d_i, best matching ground truth center g_j^* is determined. Matches for d_i, whose distances are higher than $T_R \times D(d_i, g_j^*)$, where T_R is a constant, are pruned:

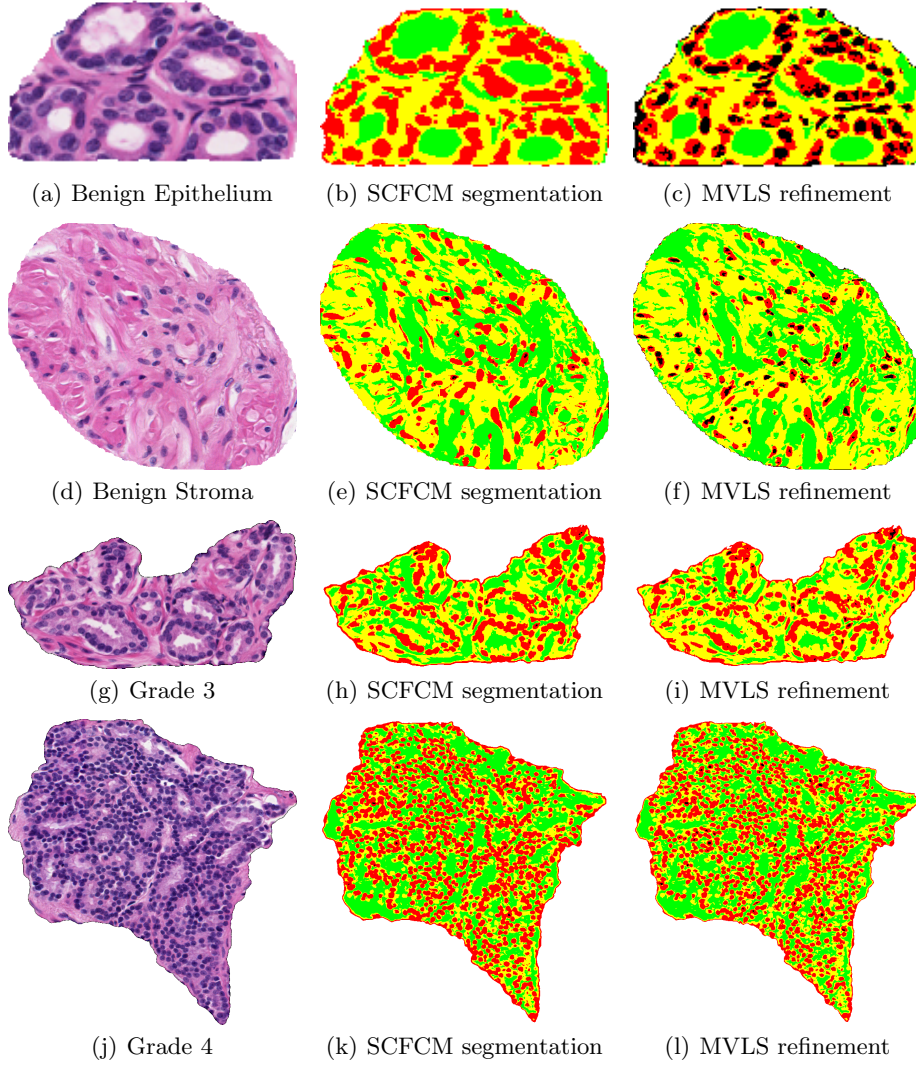$$D(d_i, g_j) > T_R \times D(d_i, g_j^*) \implies M(d_i, g_j) = 0 \qquad g_j \in 1..n_G \qquad (10)$$

The same relative pruning process is applied for each ground truth center. Using the final match matrix M one-to-one, many-to-one, one-to-many, one-to-none, or none-to-one matches are determined. Figure 5 shows detected centers, ground truth centers, and their correspondences for a sample image.

6   Results and Discussion

We have applied the proposed segmentation algorithm to histopathology images of prostate cancer tissues from four categories: benign epithelium, benign stroma, Gleason grade 3 adenocarcinoma, and Gleason grade 4 adenocarcinoma. Two images from each category were used to quantitatively evaluate the accuracy

(a) Benign Epithelium   (b) SCFCM segmentation   (c) MVLS refinement

(d) Benign Stroma   (e) SCFCM segmentation   (f) MVLS refinement

(g) Grade 3   (h) SCFCM segmentation   (i) MVLS refinement

(j) Grade 4   (k) SCFCM segmentation   (l) MVLS refinement

Fig. 6. Automatic segmentation of four tissue types (original images in column one) into three categories with nuclei shown in red and black, lumen in green, epithelial cytoplasm in yellow. Column two shows the initial segmentation using spatial constraint fuzzy c-means (SCFCM) and the final segmentation using multiphase vector-based level sets (MVLS).

of the proposed segmentation method particularly for detecting nuclei. Each image is segmented into four classes (shown in different colors in Fig. 6) for characterizing the gland structures: epithelial nuclei (red and black), lumen area (green), and epithelial cytoplasm (yellow). Fig. 6 shows original images of the four tissue types in the first column, the spatial constraint fuzzy c-means based

Table 1. Statistics of comparison between the automatic nuclei center detection and the ground truth. **GT**: ground truth centers. **DT**: detected centers. **1-to-1**: denotes one detected match with one unique ground truth. **1-to-M**: denotes one detected match with many ground truth centers. **M-to-1** denotes many detected centers match with one ground truth.

Category	#GT	#DT	#Match (1-to-1)	#Match (1-to-M)	#Match (M-to-1)	#False Negatives	#False Positives
Benign Epithelium	281	240	194(69%)	66(23%)	18(6%)	3(1%)	1(0%)
Benign Stroma	286	357	243(85%)	27(9%)	13(5%)	3(1%)	14(5%)
Grade 3	553	630	451(82%)	76(14%)	15(3%)	11(2%)	9(2%)
Grade 4	1425	1282	1136(80%)	228(16%)	55(4%)	6(0%)	8(1%)

initial segmentation in the second column and the final multiphase vector-based level set refined segmentation in the third column. The intense central regions of the nuclei are distinct enough that they are sometimes segmented into a separate class which are labeled black. In the last step the merged nuclei regions are further processed to locate individual nuclei centers using the iterative voting method described in Section 4.

The detected nuclei were compared to the ground truth annotated by medical experts. Table 1 shows statistics obtained from the evaluation process described in Section 5. The many-to-one ground truth match category means that multiple detected cells centers matched with one ground truth center (over segmentation), the opposite case is the one-to-many ground truth match category where one detected center corresponds to multiple ground truth centers (under segmentation). False positives correspond to detected center which do not exist in the ground truth. False negative correspond to missed ground truth centers.

Two useful quality measures used in other applications that we use to asses overall performance are as follows:

$$Recall = \frac{\#(true positives)}{\#(ground truth)} \quad Precision = \frac{\#(true positives)}{\#(detected centers)}$$

Table 2 shows an average recall rate of 85% and an average precision rate of 84% in terms of segmenting nuclei across the four tissue types shown in Fig. 6. It should be noted that the proposed technique works extremely well (in terms of both recall and precision) even for Gleason Grade 4 images (row 4 in Fig. 6) with the highest number and density of cell nuclei. There is also some degree

Table 2. Percentage of recall and precision for the correct detection

Category	Recall	Precision
Benign Epithelium	78%	92%
Benign Stroma	90%	72%
Grade 3	87%	77%
Grade 4	85%	95%

of inconsistency in the quality of the ground truth across experts in identifying indistinct nuclei, so that some of the false positives detected by the algorithm may indeed be correct. Further, interaction with experts is needed to refine the ground truth in order to accurately quantify segmentation performance. Overall the false negative rate and the false positive rate is less than 5.5% excluding the benign stroma case.

7   Conclusion

In this paper we described a robust algorithm for fully automatic tissue segmentation of glandular structures in histopathology imagery. An accurate unsupervised initialization is provided using the spatial constraint fuzzy c-means developed previously by our group. The initial image clusters which may not be spatially contiguous with biological regions of interest are refined using an extended active contour algorithm based on multiphase vector-based level sets to handle complex biological structures in multispectral imagery. This results in an accurate segmentation of the lumen and epithelial tissue regions. The closely spaced nuclei regions are often combined together into a single group after the level set segmentation and need to be resolved into individual nuclei centers. We use an iterative oriented kernel filtering approach to split a merged group of nuclei into multiple cell nuclei quite accurately. Our automatic tissue segmentation technique has an average recall and precision performance of 85% and 84% respectively when compared to manual ground-truth for cell nuclei centers provided by an expert. Future extensions that we are exploring include incorporating a learning process to accommodate tissue variability as well as using human annotation to improve the overall segmentation accuracy.

References

1. Doyle, S., Hwang, M., Shah, K., Madabhushi, A., Feldman, M., Tomaszeweski, J.: Automated grading of prostate cancer using architectural and textural image features. In: IEEE International Symposium on Biomedical Imaging: From Nano to Macro ISBI 2007. (April 2007) 1284–1287
2. Naik, S., Doyle, S., Feldman, M., Tomaszewski, J., Madabhushi, A.: Gland segmentation and computerized gleason grading of prostate histology by integrating low-, high-level and domain specific information. In: Proceedings of MIAAB, Piscataway, NJ, USA (2007)
3. Hafiane, A., Zavidovique, B., Chaudhuri, S.: A modified fcm with optimal peano scans for image segmentation. In: IEEE ICIP, Genova, Italy (2005)
4. Vese, L., Chan, T.: A multiphase level set framework for image segmentation using the Mumford and Shah model. *Intern. J. Comput. Vis.* **50**(3) (2002) 271–293
5. Chan, T., Vese, L.: Active contours without edges. *IEEE Trans. Image Process.* **10**(2) (Feb. 2001) 266–277
6. Mumford, D., Shah, J.: Optimal approximations by piecewise smooth functions and associated variational problems. Communication on Pure and Applied Mathematics **42** (1989) 577–685

7. Dufour, A., Shinin, V., Tajbakhsh, S., N. Guillén-Aghion, J.-C. Olivo-Marin, Zimmer, C.: Segmenting and tracking fluorescent cells in dynamic 3-D microscopy with coupled active surfaces. *IEEE Trans. Image Process.* **14**(9) (Sep. 2005) 1396–1410

8. Yan, P., Zhou, X., Shah, M., Wong, S.: Automatic segmentation of high-throughput rnai fluorescent cellular images. IEEE Trans. on Information Technology in Biomedecine **12**(1) (January 2008)

9. Caselles, V., Kimmel, R., Sapiro, G.: Geodesic active contours. Int.J. Comput. Vis. **22**(1) (1997) 61–79

10. Bunyak, F., Palaniappan, K., Nath, S.K., Seetharaman, G.: Flux tensor constrained geodesic active contours with sensor fusion for persistent object tracking. Journal of Multimedia **2**(4) (Aug 2007) 20–33

11. Chan, T., , Sandberg, B., Vese, L.: Active contours without edges for vector-valued images. J. of Visual Communication and Image Representation **11** (2000) 130–141

12. Gevers, T., Weijer, J., Stokman, H.: Color feature detection. In Lukac, R., Plataniotis, K., eds.: Color Image Processing: Methods and Applications. CRC Press (2006)

13. Parvin, B., Yang, Q., Han, J., Chang, H., Rydberg, B., Barcellos-Hoff, M.H.: Iterative voting for inference of structural saliency and characterization of subcellular events. IEEE Transactions on Image Processing **16**(3) (March 2007) 615–623

14. Schmitt, O., Hasse, M.: Radial symmetries based decomposition of cell clusters in binary and gray level images. Pattern Recognition **41** (2008) 1905–1923